Multifrequency illumination patterns in single snapshot tissue optical properties imaging

Dylan Dao, Jie Jiao

Abstract—Spatial Frequency Domain Imaging (SFDI) is an emerging optical technique that non-invasively images tissue optical properties by measuring how tissues modulate a sinusoidal illumination pattern. It requires capturing at least 3 images per spatial frequency, limiting its real-time capabilities. Here, we investigate the optimization of illumination patterns to sample tissues at multiple frequencies in a single snapshot. We investigate the effects of the angle between superimposed spatial frequencies in the Single Snapshot Multiple frequency Demodulation (SSMD) technique and conclude that 45°performs the best as it balances aliasing and padding artifacts. We also investigate the use of multiplexed patterns in the Single Snapshot Optical Properties (SSOP) technique. We find that increasing the multiplexing frequency decreases accuracy due to diffusion between multiplex boundaries, though this performance is somewhat recoverable through vertical deblurring.

1 Introduction

Tissue oxygenation is the measure of oxygen-saturated hemoglobin concentration in blood. It allows us to quantitatively assess metabolism and heart functions, and is widely used in clinics to track cardiovascular and respiratory disease progression. Since tissue behaves as a turbid media under illumination, its optical properties may be extracted from its diffuse reflectance. (De)oxygenated blood has a distinct optical signature under near-infrared (NIR) illumination, so blood oxygenation can be measured from tissue optical properties.

Spatial Frequency Domain Imaging (SFDI) is an emerging technique which takes advantage of recent advancements in Digital Micromirror Devices (DMD) and other Spatial Light Modulator (SLM) technologies to non-invasively produce wide-field images of tissue optical properties [1]. In SFDI, incident light is coded by a DMD to project 2D sinusoidal patterns onto tissue. The tissue's optical response to the illumination pattern is then collected by a camera to sample the tissue's modulation transfer function (MTF) at the modulating frequency. The tissue's MTF can be mapped to its optical properties (absorption and effective scattering coefficients, μ_a and μ_s' respectively), which are used to estimate oxygenated blood concentrations. To recover MTF, the reflected light needs to be demodulated, or measuring the amplitude envelope and DC shift of the reflected light. To demodulate in SFDI, at least 3 phase-shifted patterned images must be captured while the sample is stationary for each modulation frequency, which limits SFDI's real-time imaging capabilities.

Recent improvements of SFDI reveal the potential of demodulation with only one image, enabling real-time wide-field imaging of tissue optical properties. However, all of these SFDI-based techniques use simple illumination patterns despite the complex illumination pattern capabilities of DMDs. In our study, we analyse and extend two such methods, Single Snapshot Optical Properties (SSOP) [2] and Single Snapshot Multi-frequency Demodulation (SSMD) [3], with multiplexed and angled illumination patterns to enable and optimize single-snapshot multifrequency SFDI.

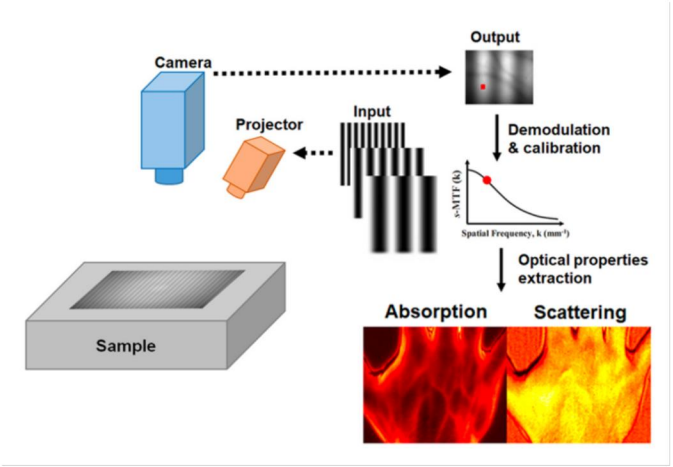

Fig. 1: Typical SFDI system. Adapted from [4].

2 Related Work

In recent years, there have been many attempts to reduce the number of images required in SFDI. SSOP technique from Vervandier et al. [2] uses low-pass and high-pass filters to extract the DC component and demodulate the AC component respectively. While this method results in more noise and depth variation artifacts, van de Giessen from the same group later used an orthogonally superimposed sinusoidal pattern to measure and correct for depth variations [5]. The Multifrequency Synthesis and Extraction (MSE) technique from Nadeau et al. projects a square wave pattern and extracts AC components from its harmonic frequencies to acquire 4 AC frequencies from 2 images with increased noise in higher-frequency harmonics [6]. The SSMD technique from Xu et al. superimposes multiple sinusoidal spatial frequencies at 45°to sample both frequencies in a single snapshot with less noise than SFDI in homogeneous samples [3], [7]. The characteristics of these SFDI variations are summarized in Tab. 1.

More broadly, similar structured light approaches have been applied to other problems in computational imaging.

TABLE 1: Summary comparison of select SFDI-based techniques.

Technique	Illumination Pattern	Demodulation	Frequencies sampled per image	Image Quality
SFDI [1]	Axis-aligned 2D sinusoidal	Averaging 3+ phase-shifted images.	2/3 = 0.67	Low noise, minimal artifacts
SSOP [2], [8]	Axis-aligned 2D sinusoidal	Low-pass/high-pass filter DC/AC components in single image	2/1 = 2.00	Moderate noise, depth-variation artifacts
SSMD [3], [7]	2 spatial frequencies superimposed at an angle	Sliding window average of unit cells.	3/1 = 3.00	Low noise in homogenous samples
MSE [6]	Axis-aligned 2D square wave	Extract harmonics of square wave to sample multiple frequencies	4/2 = 2.00	Noise/artifacts increases as sampled harmonic frequency increases

Nayar et al. demonstrates to usage of high frequency stripe patterns to separate direct and indirect light reflection in a scene [9]. O'Toole et al. uses optimized coded masks, allowing direct/indirect light separation in a single snapshot in EpiScan3D [10].

In summary, recent SFDI-based techniques have attempted to reduce the number of required images to sample the tissue's MTF at multiple spatial frequencies at the cost of increased noise and artifacts. Simultaneously, advancements in direct/indirect light separation techniques have moved beyond simple striped patterns and towards optimized coded illumination patterns. Hence, we believe that multifrequency optimized illumination patterns can be implemented in SFDI for high-quality single snapshot tissue property measurements.

3 Proposed Method

3.1 SFDI Theory

To understand how our illumination and demodulation methods differ, we first introduce fundamental SFDI theory. SFDI uses DMD modulated light to extract tissue properties. The incident pattern is a sinusoidal AC on top of a background DC, since it is impossible to create negative intensity. Formula (1) shows the x-direction modulation with single AC frequency f_x and DC intensity $I_0/2$, where I is the intensity of the illumination pattern.

$$I = \frac{I_0}{2}(\cos(2\pi f_x x) + 1) \tag{1}$$

The measured diffuse reflected light contains both DC modulation, M_{DC}, and AC modulation, M_{AC}, from the tissue MTF. With the three-phase method, the DC and AC components can be computed using formula (2) (3), where I_1, I_2, I_3 are the three phase-shifted measured images. Intuitively, we are averaging the phase shifted images to recover the DC shift and amplitude envelope.

$$M_{DC}(x_i) = \frac{1}{3}[I_1(x_i) + I_2(x_i) + I_3(x_i)] \tag{2}$$

$$\begin{aligned} M_{AC}(x_i, f_x) = \frac{\sqrt{2}}{3}\{&[I_1(x_i) - I_2(x_i)]^2 \\ &+ [I_2(x_i) - I_3(x_i)]^2 \\ &+ [I_3(x_i) - I_1(x_i)]^2\}^{1/2} \end{aligned} \tag{3}$$

For homogenous samples, M_{DC} and M_{AC} are constants over the whole image. Therefore, we can assess demodulation quality by comparing the standard deviation against the average signal. To map M_{DC}, M_{AC} to the diffuse reflectance curve $R_d(f_x)$, we normalized them to the theoretical DC illumination reflectance of a tissue phantom of known optical properties. Finally, values of $R_d(f_x)$ can be mapped to optical properties μ_a, μ_s' using a lookup table (LUT) generated from light transport simulations. In our project, we image a tissue phantom of known optical properties. Hence, we can compare our results with a theoretical curve given by formula (4) derived in [1].

$$R_d(f_x) = \frac{3Aa'}{(\mu_{eff}'/\mu_{tr} + 1)(\mu_{eff}'/\mu_{tr} + 3A)} \tag{4}$$

In the equation above, $A, a', \mu_{eff}', \mu_{tr}$ depend on intrinsic properties μ_s', μ_a', and refractive index n. This provides an opportunity to calculate the density of absorbing media such as (de)oxygenated blood in tissue based on diffuse reflectance measurements.

3.2 Illumination Patterns

Standard SFDI and SSOP uses 2D sinusoidal patterns for illumination. For our project, we explore the possibility of multiplexing frequencies in a layered pattern inspired by Nayar et al.'s high frequency stripe patterns in direct/indirect light separation [9]. Here, we test multiplexing 4 AC frequencies (0.1, 0.2, 0.3, 0.4 mm^{-1}). Our multiplexed patterns are shown in Fig. 2.

For SSMD, two sinusoidal patterns are overlapping, where each frequency is chosen specifically to form repeating unit cells. With an angle θ in between, the combined pattern can be written as formula (5):

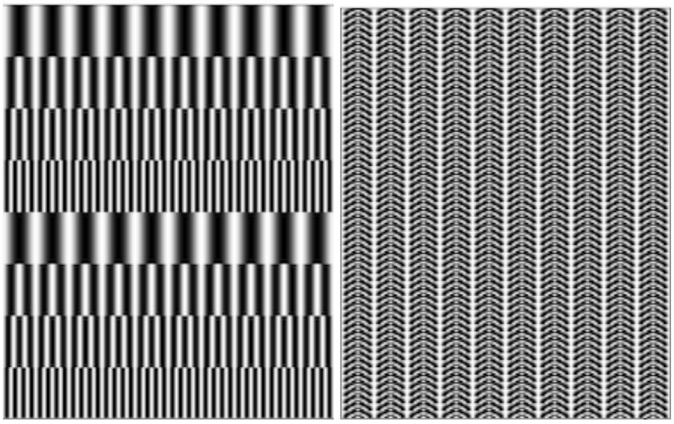

(a) 2 repetitions (b) 64 repetitions

Fig. 2: Sample multiplex pattern illumination masks programmed onto the DMD.

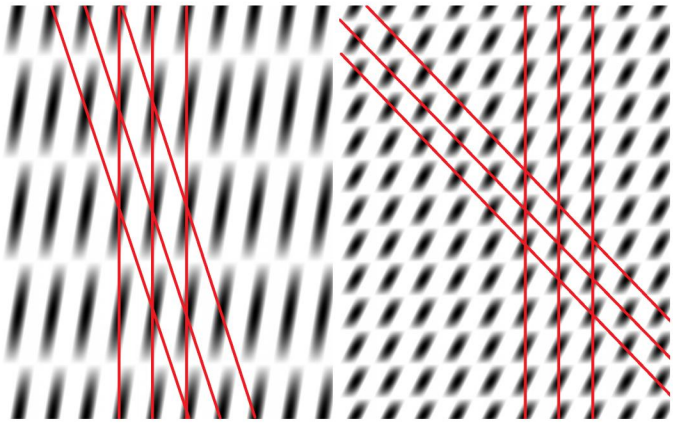

(a) 30 °overlapping (b) 60 °overlapping

Fig. 3: Sample angled pattern illumination masks programmed onto the DMD. Red lines indicate wavefronts of superimposed frequencies.

$$\begin{aligned} I_1 &= \frac{I_0}{2}(cos(2\pi f_x x) + 1), \\ I_2 &= \frac{I_0}{2}(cos(2\pi f_d d) + 1), \\ I_{angled} &= I_1 + I_2 \end{aligned} \tag{5}$$

Where I_2 is the tilted pattern, whose wave function is linked with θ in formula (6).

$$\begin{aligned} f_d &= \frac{f_x}{\cos\theta}, \\ d &= \cos\theta x + \sin\theta y \end{aligned} \tag{6}$$

The resulting pattern is shown in Fig. 3, where red lines indicate wavefronts of each component (angles in the produced patterns are not exact due to DMD pixel shape, but the projected patterns will have exact 30°and 60°angles).

We also examine the effects of multiplexing more frequencies in a single image, or overlapping two patterns with different angles (15°, 30°, 45°, 60°, 75°) in between. More details about which pattern is the optimum are presented in Section 4.1.

3.3 Demodulation Methods

Due to our modified illumination patterns, our demodulation methods must also change appropriately. We describe them in this section.

3.3.1 *Multiplex SSOP*

Our variation of SSOP using vertically multiplexed spatial frequencies involves a vertical deblurring step followed by line-by-line deconvolution by low/high-pass filtering.

Since the goal of SFDI is to sample tissue properties by how tissue modulates a projected illumination pattern, the blur resulting from diffuse reflectance contains important optical information that cannot be filtered. However, blurring the boundaries between different regions of spatial frequencies is undesirable as it causes low frequencies to bleed over boundaries and overpower high frequency reflectance (Observed in Section 4.3). Therefore, we apply Maximum Likelihood Deconvolution (MLD) [11] to each column of pixels (orthogonal to spatial frequency pattern direction) independently to estimate and deconvolve a 1x15 vertical blurring PSF. This allows us to preserve the horizontal diffusion blurring while sharpening the boundaries between multiplexed spatial frequencies.

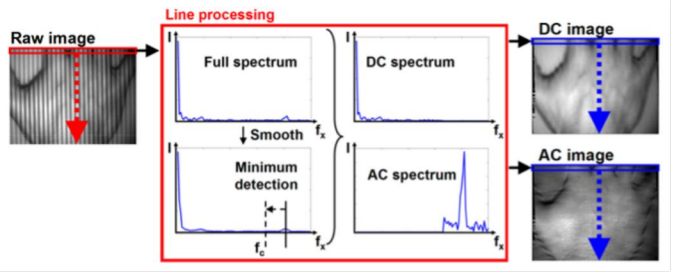

Fig. 4: SSOP demodulation process from [2].

Using the vertically-deblurred images, we apply line-by-line SSOP as described by Vervandier et al. [2]. For each horizontal line of pixels in the captured image, we compute the Fast Fourier Transform (FFT). Then, we detect the strongest AC frequency peak (2nd highest peak after the DC peak) assumed to be the spatial frequency projected onto that line. We then apply an ideal low-pass filter to extract the DC spectrum of the line, and an ideal one-sided high-pass filter with cutoff frequency f_c corresponding to the nearest local minimum to the AC peak. We then compute the Inverse Fast Fourier Transform (IFFT) of the DC/AC spectrums to recover DC/AC images. We note that due to the one-sided high-pass filter, the AC peak is demodulated after IFFT (shifted to fx=0). Fig. 4 visualizes the deconvolution process.

3.3.2 *SSMD*

For SSMD, the demodulation is performed with a sliding window about each pixel. It can be noticed from the pattern that rectangular repeating boxes exist. DC and AC can be extracted pixel-by-pixel using formula (7).

In formula (7), σ represents the area enclosed by the box around each pixel, with $T_1 = 1/f_x, T_2 = 1/f_y$. It also implies I_{DC} to be the average signal strength inside the box,

$$I_{AC,i} = \frac{\sqrt{[\iint_{\sigma} I(x,y)\cos(2\pi f_{x,i}x + 2\pi f_{y,i}y)dxdy]^2 + [\iint_{\sigma} I(x,y)\sin(2\pi f_{x,i}x + 2\pi f_{y,i}y)dxdy]^2}}{\iint_{\sigma} \cos^2(2\pi f_{x,i}x + 2\pi f_{y,i}y)dxdy},$$
$$I_{DC} = \frac{1}{T_1 \times T_2}\iint_{\sigma} I(x,y)dxdy. \tag{7}$$

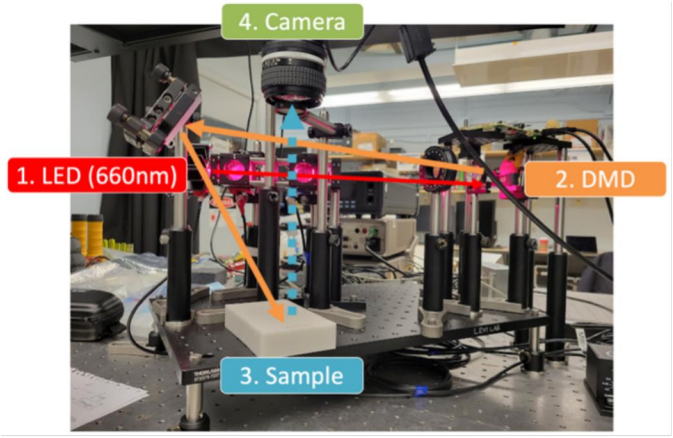

Fig. 5: SFDI optical setup developed by Kuramoto [12]. Optical path is drawn with coloured arrows corresponding to originating component labels.

while I_{AC} is the average strength of the alternating signal of the given frequency. The sliding window size, $T_1 \times T_2$, also represents resolution of this method.

TABLE 2: Imaging parameters.

Rolera EM-C^2 CCD Camera (QImaging)	Sensor size	8x8 mm
	Pixel size	8x8 μm
	Resolution	1004x1002 px
	Field of View (FoV)	6 x 6 cm
Lens (Nikon)	Focus distance	26 cm
	Focal length	28 mm
	Aperature size	f/2.8
	Physical Length per camera pixel	0.11 mm/px
DLP 4500 DMD (Texas Instruments)	Surface size	8.7x6.9 mm
	Pixel size	7.6x7.6 μm
	Resolution (diamond px)	1140x912 px
	Physical length per DMD pixel	0.06 mm/px
Optical Path	Illumination path magnification	25x
	Imaging path magnification	0.133x

TABLE 3: Tissue phantom optical properties at 660 nm.

Index of Refraction n	1.5111
Absorption Coefficient μ_a [mm^{-1}]	0.0255
Reduced Scattering Coefficient μ_s' [mm^{-1}]	1.26
Anisotropy g	0.62

3.4 Experimental Setup

3.4.1 Optical Setup

This work utilizes an existing SFDI optical setup developed by Kuramoto et al. from our group, based on the open-source SFDI guide OpenSFDI [12], [13]. Fig 5 shows a labelled diagram of this setup. While the diagram image is taken with lights on for visual clarity, experiments were conducted in the dark to minimize ambient lighting on the tissue phantom. A 660nm LED illuminates a DLP 4500 DMD (Texas Instruments) to project our illumination patterns. The projected patterns are magnified 25x with a convex lens and reflected by a mirror onto the sample, imaged by an overhead Rolera EM-C^2 EM-CCD camera (QImaging) equipped with a camera lens (Nikon) placed 26 cm away from the sample. This is done so that the DMD patterns are sufficiently large to maximize illumination area on the sample as well as maximize camera FoV coverage. To reduce specular reflections from the tissue phantom, we introduce crossed polarizers between the illuminating pattern and the camera. Relevant optical setup parameters are shown in Tab. 2.

3.4.2 Calibration

Not only must the camera be focused on the sample; the magnified illumination pattern must also be sufficiently sharp when projected onto the tissue as SFDI-based techniques predicts tissue properties from how tissues blur projection patterns. The camera lens is focused onto the sample by adjusting the focus ring until ruler lines on top of the sample are the sharpest. The illumination path is focused by projecting a grid pattern with the DMD and adjusting until the x and y intensity profiles are the sharpest and most uniform. We note that due to the tilt of the mirror, projected patterns warp at the edges of the pattern and the projected intensity drops near the bottom edge of the captured image.

3.4.3 Image Capture/Pre-Processing

For each pattern, 100 14-bit 501x502 pixel images (2x binning) are successively taken with 100 ms exposure and averaged to remove read/shot noise effects. To remove pattern distortions at the edges of images, we crop to the center 300x300. Due to the high alignment sensitivity of the multiplex pattern SSOP method, these images are digitally unrotated to align patterns to the image coordinate axes.

3.4.4 Sample

We image a diffuse homogenous tissue phantom with optical properties summarized in Tab. 3.

3.4.5 Assessment

To assess our methods' fit to theoretical expectations, we compare measured reflectances against the diffusion approximation described by Formula (4). We also include 3-phase SFDI (provided in OpenSFDI [13]) and Vervandier

et al.'s SSOP [2] as representative single spatial frequency techniques in both multiple image and single snapshot varieties for comparison. To normalize the 14-bit image pixel intensities to diffuse reflectance values, we normalize each curve such that the DC reflectance ($f_x = 0$) matches the theoretical DC expectation as described in Section 3.1.

3.4.6 Software

SFDI/SSOP-based and SSMD-based methods are implemented and analysed in MATLAB r2022b (Mathworks) and Python 3.7 respectively.

4 Experimental Results

Fig. 6 shows the measured reflectance curves of our implementations of SSMD and multiplexed SSOP alongside 3-phase SFDI, SSOP. A theoretical curve from the diffusion approximation (Formula (4)) is also shown to serve as the ground truth. Each point corresponds to the average reflectance value of pixels associated with each spatial frequency with error bars representing the standard deviation.

4.1 SSMD Angle Optimization

To compare results of changing angles and locate the best angle for reflectance measurement, we fix f_x = 0.1mm^{-1}, while making patterns with 15°, 30°, 45°, 60°and 75°angles between the two components. The resulting images, together with their respective AC and DC signals, are shown in Fig. 7.

By comparing the demodulation results, we conclude that standard deviation is about 3-4% for all the aforementioned angles. However, for angles smaller than 45°, the overlapping patterns have similar frequencies, which makes it difficult to extract R_d information through the whole f_x spectrum. In addition, The sliding window size is larger for smaller angles, which extends the edge artifacts deep into the image, and reduces its resolution. On the other hand, there is noticeable amount of aliasing artifacts for larger angle patterns. For example, in the 75°angle pattern, the vertical fluctuation is so dense that there may not be enough DMD pixels to fit the sine function well. In general, we choose 45°to be the optimum angle for diffuse reflectance measurement, and the MTF curve for SSMD is therefore constructed based on 45°patterns with varying spatial frequencies.

4.2 SSMD Frequency Sweep

From theoretical curve in Fig. 6, we notice that R_d approaches 0 mm^{-1} as frequency goes over 0.5 mm^{-1}. For the 45°arrangement, the spatial frequency of the tilted pattern can be calculated by formula (8).

$$f_d = \sqrt{2} f_x \tag{8}$$

Under this relationship, we choose f_x to be 0.06, 0.10, 0.20, 0.30 mm^{-1}, which gives the secondary frequency to be 0.08, 0.14, 0.28, 0.42 mm^{-1}. This selection of frequencies provides an even distribution of sweeping, so we may draw a more precise curve to reflect the trend. The resulting reflectance for each f_x after running demodulation and calibration for the prepared patterns is included in Fig. 6.

4.3 Pattern Multiplexing with Vertical Deblurring

First, we consider the simplest multiplexed pattern case as seen in the first column of Fig. 8, in which the spatial frequencies are 0.1, 0.2, 0.3, 0.4 mm^{-1}, with each region vertically spanning 10 mm. As can be seen in the reflectance curve in Fig. 6, the yellow SSOP curve and the green Multiplex SSOP curve are nearly identical. In other words, the average reflectance computed from ¼ of a homogenous tissue phantom image (75x300) is nearly as accurate as when computed with four separate 300x300 images. While this pattern would be ineffective for inhomogeneous samples (for a hand, the tips of the fingers and base of the hand would be sampled at a single discrete frequency), it implies that 300x300 images can support sampling at 4 spatial frequencies simultaneously provided each spatial frequency occupies 75 1x300 pixel lines.

To support 4 AC frequency sampling of inhomogeneous samples, we spread each spatial frequency pattern across the entire FoV by increasing the frequency at which patterns switch. Column 2 in Fig. 8 shows 256 regions with a vertical span of 0.1 mm. Without vertical deblurring, this results in a reflectance curve that significantly underestimates the reflectance at all AC frequencies. Furthermore, no lines of the image are registered to 0.4mm^{-1}, resulting in missing data at that spatial frequency. In the spectrum in Fig 9, we see that the 0.4mm^{-1} peak is small compared to the lower frequencies despite a 0.4 mm^{-1} frequency being projected onto that line. Furthermore, in the histogram presented in Fig. 10, we see that the number of lines associated to a spatial frequency decreases as spatial frequency increases. This occurs due to the tissue phantom diffusing lower frequencies across boundaries of adjacent regions. While we desire blurring in the x-axis of the image as it represents the optical tissue response, diffusion in the y-axis causes low frequencies to bleed into high frequency regions, negatively impacting frequency registration and therefore undermining reflectance measurement.

The measurement is somewhat recoverable after vertical deblurring (Fig 8, 3rd column). In Fig. 9, we see that the strength of the 0.4 mm^{-1} peak is recovered while the width of the peak representing the tissue response is maintained. We also see in Fig. 10 that while we still see frequency misregistration skewing the counts to lower spatial frequencies, we can now detect the 0.4mm^{-1} regions. In the reflectance curve in Fig 6, we see that while it still performs notably worse than SSOP, the reflectance curve accuracy is somewhat improved compared to without vertical deblurring.

In summary, increasing the multiplexing frequency allows us to sample the entire FoV with all spatial frequencies but decreases the accuracy of reflectance measurement due to tissue diffusion blurring the boundaries between different spatial frequency regions. We have shown that this is somewhat recoverable with our vertical deblurring method.

5 Discussion

The conclusions of the following sections are summarized in Tab. 4.

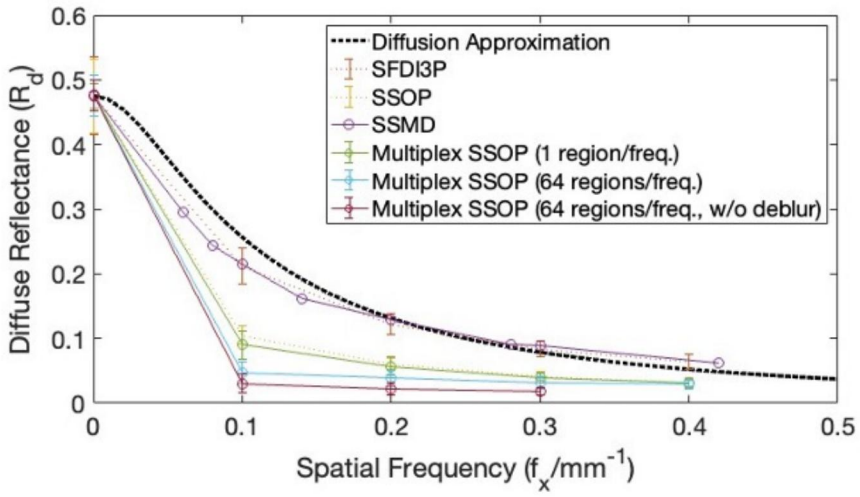

Fig. 6: Average diffuse reflectance by spatial frequency of homogenous tissue phantom images from the SFDI-based methods described in this report.

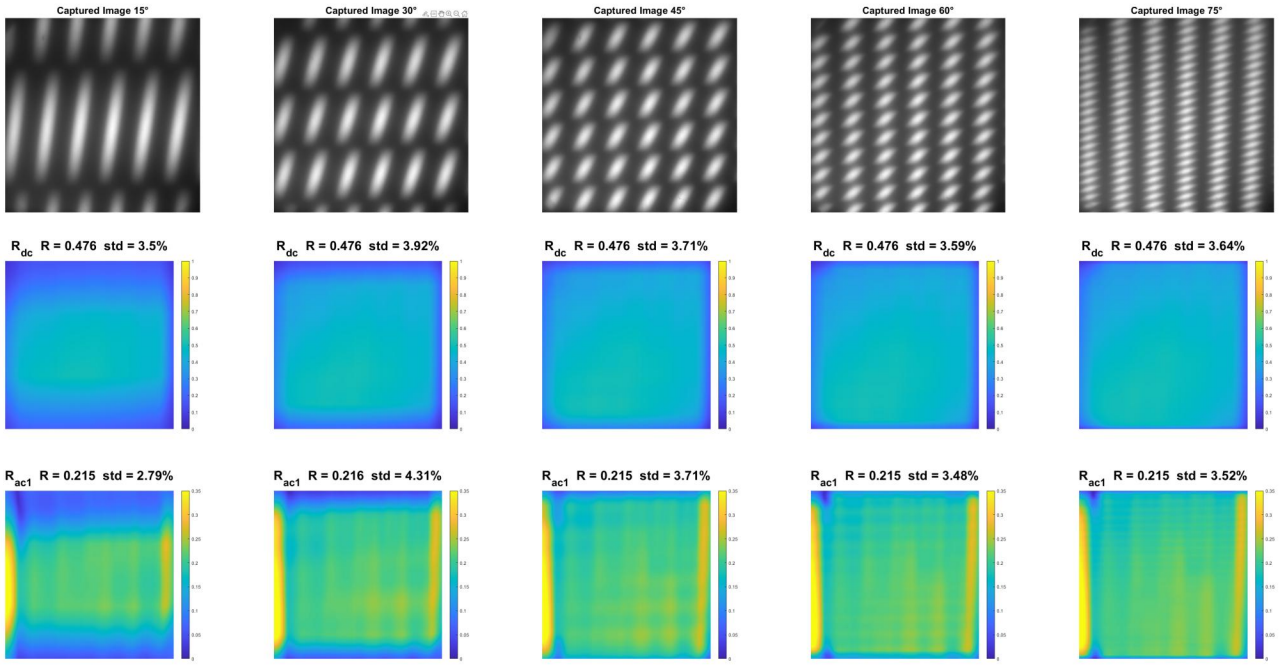

Fig. 7: DC and AC results of different angle patterns.

TABLE 4: Summary of assessment of SFDI-based techniques explored in this report.

Technique	R_d Accuracy	Efficiency (f/img)	Uniformity	Complexity
SFDI	High	0.67	High	$O(n)$
SSOP	Moderate	2.00	Moderate	$O(n \log n)$
SSMD	High	3.00	High	$O(n^2)$
Mux. SSOP	Moderate	5.00	Low	$O(n \log n)$

5.1 Accuracy

For discussion, we assume the diffuse approximation result to be the theoretical truth. From Fig, 6, 3-phase SFDI and SSMD agree better with the theory, while SSOP methods have relatively larger error. Since SFDI and SSMD both extract DC signal strength based on the average tissue response, low-frequency noise does not significantly affect reflectance measurements. However, such noises contribute to near-origin signal in the Fourier domain, and mix with the DC signal in the SSOP process. As a consequence, demodulated DC is higher than the actual DC value, which leads to a larger normalization factor in the calibration

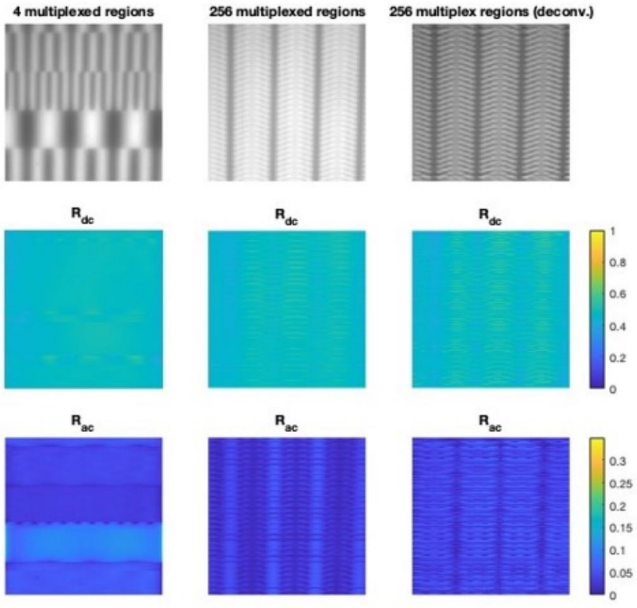

Fig. 8: Tissue phantom illuminated by select multiplexed patterns (top row) with SSOP recovered DC/AC reflectance maps (middle/bottom row).

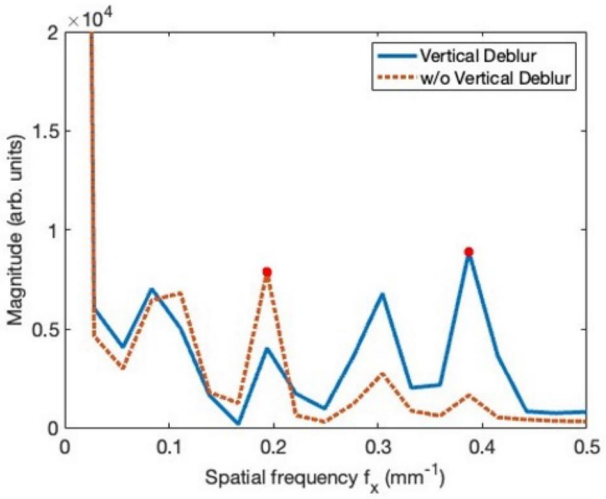

Fig. 9: Sample frequency spectrum of a single line in the 256 region image with and without vertical deblurring. Red dots mark the strongest AC frequency on each spectrum.

process, dragging down the AC signal values.

The same phenomenon of low-frequency reflectance being smaller then expected is also observed for SFDI and SSMD. There are two potential sources for this inaccuracy. First, our optical setup may not be able to remove all specular reflectance. In practice, it is impossible to illuminate the phantom directly from above, otherwise the mirror would block the FoV of camera. The small incident angle causes the specular reflected light to possess a small z-polarization, which cannot be completely removed with x and y cross-polarizers in our experimental setup. Second, tissue phantom acts as a low-pass filter [14], meaning low-frequency light is less attenuated after multiple scattering events. Since AC signals have non-zero spatial frequencies,

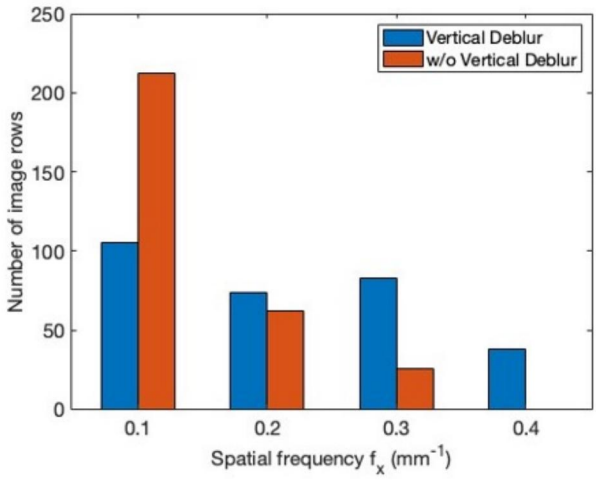

Fig. 10: Distribution of spatial frequencies associated with each of 300 lines in the 256 region image with and without vertical deblurring.

which are more absorbed by the phantom than DC signals, we may collect higher DC signal strength than the theory predicts. In general, SSMD results coincide with SFDI, which has a maximum error about 15% from the theoretical curve. Comparatively, 4-region SSOP gives similar results to standard SSOP, whose maximum inaccuracy is about 50%, while 256-region SSOP gives a >80% maximum inaccuracy.

5.2 Efficiency

We define efficiency to be the number of frequencies that can be demodulated per image taken. For both standard SFDI and SSOP, there is only one AC signal over a DC shift, which means we can only extract two independent signals. However, since SFDI requires 3 phases of the same pattern for complete demodulation, its efficiency is 2/3 = 0.67. For SSOP, only one snapshot is taken, leading to a higher efficiency of 2/1 = 2.00. In SSMD, the illumination pattern consists of 2 ACs and 1 DC signals, which is also able to be demodulated with only one snapshot, resulting in an efficiency of 3/1 = 3.00. Finally, for multiplex SSOP, we could theoretically overlay as many frequencies as possible depending on how large the multiplexed regions are. In our project we multiplex up to 5 frequencies (4 AC, 1 DC), so efficiency is 5/1 = 5.00. In conclusion, novel methods of SFDI aim to sample the tissue at as many spatial frequencies as possible in a single snapshot. Although multiplex SSOP has relative low accuracy, it has the potential to combine more frequencies, which may be an advantage if more accurate demodulation techniques are found in the future.

5.3 Uniformity

From our results, we notice a huge difference between the standard derivation of different methods, and we define this parameter as demodulation uniformity. For more complete demodulation, the resulting DC and AC would more uniformly span the image, which leads to a smaller standard deviation. From Fig. 7, the percentage fluctuation in SSMD is about 3-4%, which is the smallest among all methods.

However, we note that SSMD uses a relatively large sliding window for averaging, which suggests that it performs best for homogeneous samples. For inhomogeneous media, SSMD may fail to extract local optical features. In comparison, standard SFDI has about 20% uncertainty. This might be due to the fact that using three phases is the minimum requirement for demodulation, and uncertainty could be reduced by using more phases (e.g 5 or 7 phases demodulation). SSOP methods, on the other hand, give the worst uniformity in demodulation, since their standard deviation is about 50% of the mean value. With 64 regions and vertical deblurring, the result is moderately improved, but there still exists a considerable amount of non-uniformity due to frequency misregistration.

5.4 Computational Complexity

SFDI is the fastest among the methods. From formula (2) and (3), its complexity is $O(n)$, as only weighted means are calculated. SSOP requires an FFT to be computed for each line of the image to filter out desired spatial frequencies, which has a complexity of $O(n \log n)$. Its improved version, multiplex SSOP, also has the same complexity, but it takes somewhat longer to compute if deblurring is applied. SSMD has the slowest speed among all these methods. For each pixel, a sliding window which has a size comparable to the whole image is swept, which means it has complexity $O(n^2)$. The speed is also dependent on the window size. For a smaller angle as shown in Fig. 7, the height of window is larger with the width fixed, which increases the total number of steps for demodulation. The complexity is ranked as follows: SFDI $<$ SSOP $<$ Multiplex SSOP $<$ SSMD.

6 Conclusion

In our project, we test different single snapshot SFDI methods in measuring the diffuse reflectance of a homogeneous tissue phantom, and compare them based on their accuracy, efficiency, demodulation uniformity and complexity. We conclude that 45°SSMD has the best accuracy and uniformity despite being a single snapshot technique extracting 3 frequencies at once. However, its computational time is the longest, limiting real-time capabilities. SSOP is another single snapshot variation of SFDI, but it suffers from low accuracy and high uncertainty. Our method, multiplex SSOP, enables multifrequency extraction, but its accuracy is limited due to diffusion over multiplex boundaries. We also show that this accuracy is somewhat recoverable with vertical deblurring. In our future work, we hope to investigate overlaying more frequencies in the SSMD approach, as well as develop better demodulation algorithms to improve accuracy in multifrequency SSOP.

Acknowledgments

We would like to thank Dr. Ofer Levi for regular guidance in experimental technique and analysis, Lindsay Kuramoto (PhD Cand.) for development and traning with the SFDI optical setup, Dr. David Lindell for providing mentorship and feedback on project direction, and Matthew Downing (MASc Cand.) for providing valuable suggestions for image analysis.

References

[1] D. J. Cuccia, F. Bevilacqua, A. J. Durkin, F. R. Ayers, and B. J. Tromberg, "Quantitation and mapping of tissue optical properties using modulated imaging," *Journal of Biomedical Optics*, vol. 14, no. 2, p. 024012, 2009 Mar-Apr.

[2] J. Vervandier and S. Gioux, "Single snapshot imaging of optical properties," *Biomedical Optics Express*, vol. 4, no. 12, pp. 2938–2944, Dec. 2013.

[3] M. Xu, Z. Cao, W. Lin, X. Chen, L. Zheng, and B. Zeng, "Single snapshot multiple frequency modulated imaging of subsurface optical properties of turbid media with structured light," *AIP Advances*, vol. 6, no. 12, p. 125208, Dec. 2016.

[4] S. Gioux, A. Mazhar, and D. J. Cuccia, "Spatial frequency domain imaging in 2019: Principles, applications, and perspectives," *Journal of Biomedical Optics*, vol. 24, no. 7, p. 071613, Jun. 2019.

[5] M. van de Giessen, J. P. Angelo, and S. Gioux, "Real-time, profile-corrected single snapshot imaging of optical properties," *Biomedical Optics Express*, vol. 6, no. 10, pp. 4051–4062, Oct. 2015.

[6] K. P. Nadeau, T. B. Rice, A. J. Durkin, and B. J. Tromberg, "Multifrequency synthesis and extraction using square wave projection patterns for quantitative tissue imaging," *Journal of Biomedical Optics*, vol. 20, no. 11, p. 116005, Nov. 2015.

[7] Z. Cao, W. Lin, X. Chen, B. Zeng, and M. Xu, "Real-time spatial frequency domain imaging by single snapshot multiple frequency demodulation technique," in *Optical Tomography and Spectroscopy of Tissue XII*, vol. 10059. SPIE, Feb. 2017, pp. 92–97.

[8] E. Aguénounon, F. Dadouche, W. Uhring, N. Ducros, and S. Gioux, "Single snapshot imaging of optical properties using a single-pixel camera: A simulation study," *Journal of Biomedical Optics*, vol. 24, no. 7, p. 071612, 2019.

[9] S. K. Nayar, G. Krishnan, M. D. Grossberg, and R. Raskar, "Fast separation of direct and global components of a scene using high frequency illumination," *ACM Transactions on Graphics*, vol. 25, no. 3, pp. 935–944, Jul. 2006.

[10] M. O'Toole, S. Achar, S. G. Narasimhan, and K. N. Kutulakos, "Homogeneous codes for energy-efficient illumination and imaging," *ACM Transactions on Graphics*, vol. 34, no. 4, pp. 1–13, Jul. 2015.

[11] D. S. C. Biggs and M. Andrews, "Acceleration of iterative image restoration algorithms," *Applied Optics*, vol. 36, no. 8, pp. 1766–1775, Mar. 1997.

[12] L. Kuramoto, "Remote tissue oxygenation monitoring using spatial frequency domain imaging and depth sensors," Master's thesis, University of Toronto, 2022.

[13] M. B. Applegate, K. Karrobi, J. P. Angelo Jr., W. Austin, S. M. Tabassum, E. Aguénounon, K. Tilbury, R. B. Saager, S. Gioux, and D. Roblyer, "OpenSFDI: An open-source guide for constructing a spatial frequency domain imaging system," *Journal of Biomedical Optics*, vol. 25, no. 1, p. 016002, Jan. 2020.

[14] T. D. O'Sullivan, A. E. Cerussi, B. J. Tromberg, and D. J. Cuccia, "Diffuse optical imaging using spatially and temporally modulated light," *Journal of Biomedical Optics*, vol. 17, no. 7, p. 071311, Jul. 2012.